What processes contribute to the spring and fall bloom co-variability on the Eastern Bering Sea shelf?

Wei Cheng[a,b*], Enrique Curchitser[c,d], Charles Stock[e], Albert Hermann[a,b], Edward Cokelet[b], Calvin Mordy[a,b], Phyllis Stabeno[b], Gaelle Hervieux[c], Frederic Castruccio[c,f]

[a]Joint Institute for the Study of the Atmosphere and Ocean, University of Washington, 3737 Brooklyn Ave NE, Box 355672, Seattle, WA 98105, USA

[b]Pacific Marine Environmental Laboratory, NOAA, 7600 Sandpoint Way NE, Seattle, WA 98115, USA

[c]Department of Environmental Sciences, Rutgers University, 14 College Farm Rd., New Brunswick, NJ 08901 USA

[d]Institute of Marine and Coastal Sciences, Rutgers University, 71 Dudley Rd., New Brunswick, NJ 08901 USA

[e]Geophysical Fluid Dynamics Laboratory, NOAA, 201 Forrestal Road, Princeton, NJ 08540-6649, USA

[f]National Center for Atmospheric Research, Boulder, CO 80305 USA

[*] Corresponding Author
wei.cheng@noaa.gov, Phone: (206) 526-4581, Fax: (206)526-6485

Abstract

Observations indicate that spring and fall phytoplankton blooms on the eastern Bering Sea (EBS) continental shelf tend to co-vary on inter-annual scales – that is, a year with a strong spring bloom also tends to have a strong fall bloom. Similar co-variability of primary production is also seen in the multi-year (1987-2007) integration of a coupled physical-biological model. Moreover, the modeled seasonal amplitudes of 10-meter chlorophyll-a concentration at the EBS middle shelf mooring locations, computed using the canonical Redfield ratio and a mean carbon-to-chlorophyll-a ratio, are generally consistent with the *in situ* mooring measurements. The coupled physical-biological model simulation is used to examine the relative contributions of wind mixing, local nutrient recycling/regeneration, horizontal nutrient advection, and water column stability to this co-variability. The main conclusions are: 1) There is no significant correlation between the spring and fall surface wind mixing. Although wind mixing is an important mechanism for bringing nutrients in the lower water column to the surface layers, it is not the mechanism tying the two seasons' productivity together. 2) Local regeneration/recycling of the nutrients initially fueling spring production is an important mechanism for spring-to-fall nutrient accumulation in the bottom layers at the middle shelf. 3) Horizontal advection does not appear to be the dominant factor for supplying nutrients to the middle shelf during the spring-to-fall period. 4) Fall primary production in the model is strongly influenced by the lower water column stability/stratification. Taken together, these results highlight the importance of local recycling/regeneration of nutrients assimilated by spring phytoplankton bloom in linking together the spring and fall primary productions on EBS middle shelf.

***Keywords*:** sea ice, phytoplankton bloom, primary production, nutrient, numerical model

1. Introduction

The Bering Sea is a subarctic marginal sea bounded to the north by the Bering Strait, and to the south by the Aleutian Island chain (Fig. 1). It has a wide (~500 km) and relatively flat (with depth less than 180 meters) continental shelf to the east and a deep ocean basin to the west. The Eastern Bering Sea (EBS) shelf is highly productive because of interactions between the ocean, sea ice, and atmospheric forcing. For example, the shelf break of the EBS is known as the "greenbelt" (Springer et al., 1996), where upwelled nutrients from the ocean basin provide fuel for phytoplankton primary production. Seasonal sea ice is another important control on productivity in the EBS. Sea ice can form in the northern EBS as early as November, and under prevailing winds, is transported southward (e.g., Pease 1980; Danielson et al., 2011; Sullivan et al., 2014). In years with extensive sea ice, the ice can cover much of the EBS shelf in March — the month typically with the maximum ice extent, but maximum ice cover can occur as early as February or as late as April (Stabeno et al., 2012a). During the melting season, sea ice retreats generally from south to north, and by mid-June the Bering Sea is usually ice free.

Sea ice extent in the EBS is highly variable on inter-annual timescales (Brown et al., 2011). During extensive ice years, with sea ice persisting on the southern shelf (south of 60° N) after mid-March, the water column over the southern shelf tends to be colder and fresher than during years with little ice (Coachman and Shigaev, 1992; Stabeno et al., 2010, 2012b; Ladd and Stabeno, 2012; Sullivan et al., 2014). The timing of ice retreat influences the timing of the spring phytoplankton bloom (Brown and Arrigo, 2013; Stabeno et al., 2012b; Sigler et al., 2014), zooplankton species composition (Eisner et al., 2014), and fish recruitment (Hunt et al., 2002, 2011; Hollowed et al., 2012). A fall

(September to early October) bloom is also common in the EBS. Using the multi-year (1995-2011) fluorescence data obtained from the long-term monitoring moorings on the EBS middle shelf (M2, M4, M5, and M8; see Fig. 1), Sigler et al. (2014) found correlations between the magnitudes of the spring and fall blooms, that is, a year with a strong spring bloom also tends to have a strong fall bloom, but the observational data are too sparse by themselves to reveal the underlying mechanisms.

In addition to ocean *in situ* and remote sensing measurements, biophysical modeling is used to examine physical and biological linkages between the ocean environment and ecosystem responses in the EBS (e.g., Jin et al., 2006, 2007, 2009; Gibson and Spitz, 2011). One such modeling system is the Regional Ocean Modeling System (ROMS) coupled to the NEMURO planktonic ecosystem model (Kishi et al., 2007) for the Northeast Pacific (NEP) (hereafter called ROMS-NEMURO NEP). A previous version of the model was used for a biophysical model developed under the Bering Sea Project (Gibson and Spitz, 2011; Gibson et al., 2013; Hermann et al., in press), also known as the Bering Ecosystem Study-Bering Sea Integrated Ecosystem Research Program (BEST-BSIERP; Sigler et al., 2010). The physical performance of the model is described in Curchitser et al. (2005), Curchitser et al. (2010) and Danielson et al. (2011).

The primary goal of this study is to examine processes influencing seasonal variability of primary production on the EBS middle shelf and, particularly, to explore mechanisms responsible for the co-variability of spring versus fall bloom amplitudes as suggested by mooring observations. Spring phytoplankton bloom dynamics on the EBS shelf have been studied extensively (e.g., Mathis et al., 2010; Brown and Arrigo, 2013;

Banas et al., this issue) while fall bloom dynamics have received comparatively less attention (Sigler et al., 2014). To achieve the above goal we focus on mechanisms that influence nutrient supply to the region in the fall — surface wind mixing, local recycling of nutrients from spring production, horizontal advection of nutrients, and water column stability. Undoubtedly, other factors than those listed above can additionally influence primary production on the EBS shelf on various time scales. Focusing on a few key processes is only the first step toward a better understanding of controlling mechanisms.

The remainder of the paper is organized as follows. In Section 2, we first introduce the data used in our analyses — mooring observations, satellite measured sea-ice concentrations, and the ROMS-NEMURO NEP biophysical model and its output, followed by descriptions of model diagnosis metrics. Main results from this study are described in Section 3. This includes model-observation comparison and an examination of possible mechanisms connecting the spring and fall blooms. In Section 4, we discuss caveats of this study and the implications of our results. Main conclusions are summarized in Section 5.

2. Data and analyses

2.1. Mooring data and satellite ice concentration

The four moorings (Fig. 1) used in this study are described in detail in Stabeno et al. (2012a, b). They are located along the 70-meter isobath on the EBS shelf. These biophysical moorings (M2, M4, M5, and M8) are maintained by NOAA/PMEL, and the first moorings at M2 were deployed in 1995. In general, they are subsurface moorings (except M2 in the summer, which is a surface mooring). Each mooring measures

temperature at ~5 m resolution through most of the water column, salinity at 3-5 depths distributed through water column, and chlorophyll-a fluorescence at ~11 m depth in south and at ~20 m at M8. The raw data were collected hourly. Daily averages of the chlorophyll-a concentration from these moorings are presented in Sigler et al. (2014), and these daily mooring chlorophyll-a data will be used in this study.

Monthly sea ice concentrations in a 100km by 100km box surrounding each mooring location are computed from the daily Bootstrap Algorithm files available at the National Snow and Ice Data Center (ftp://sidads.colorado.edu/pub/DATASETS/nsidc0079_gsfc_bootstrap_seaice/final-gsfc/north/daily/). We use the overlapping years (1987-2007) between the satellite data and the ROMS-NEMURO NEP simulation (described in the next subsection) in our analysis. The daily files use data from the Scanning Multichannel Microwave Radiometer (SMMR) aboard the Nimbus-7 satellite or the Special Sensor Microwave/Imager (SSM/I) aboard Defense Meteorological Satellite Program (DMSP) satellites (Comiso, 2002, updated 2014), depending on the year.

2.2 The coupled physical-biological model

The ROMS-NEMURO NEP model used in this work is the sixth generation of the ROMS implementation in the Northeast Pacific previously described in Curchitser et al., (2005, 2010), Hermann et al. (2009 a,b), and Danielson et al. (2011). It is based on the Regional Ocean Modeling System (Shchepetkin and McWilliams, 2005) coupled with a sea ice component (Budgell, 2005) and a modified implementation of the NEMURO plankton ecosystem model (Kishi et al., 2007). Significant differences in the physics

from previous implementations include spatially and temporally variable fresh water inputs based on the Dai et al. (2009) dataset and spatially variable bottom drag and water column light absorption.

The sea-ice model (Budgell, 2005) consists of the elastic-viscous-plastic (EVP) rheology (Hunke and Dukowicz, 1997; Hunke, 2001) and the Mellor and Kantha (1989) thermodynamics. No light penetrates below the sea ice. The sea-ice model also includes frazil ice growth in the ocean (Steele et al., 1989). It currently follows a single ice thickness category, which exhibits accurate results in a seasonally ice-free region such as the Bering Sea (Danielson et al., 2011).

The basic NEMURO plankton ecosystem model (e.g., Kishi et al., 2007; Fiechter et al., 2009, 2014) includes components for nitrogen, silica, small and large phytoplankton and small, large and predatory zooplankton groups. The NEMURO state variables are nitrate (NO_3), ammonium (NH_4), small phytoplankton (PS), large phytoplankton (PL), small zooplankton (ZS), large zooplankton (ZL), predatory zooplankton (ZP), particulate organic nitrogen (PON), dissolved organic nitrogen (DON), particulate organic silicon (Opal), and silicic acid ($Si(OH)_4$). All state variables except silica are in the units of mmol N/m^3. For the current implementation, modifications to the NEMURO model include small phytoplankton and small zooplankton parameter adjustments described in Kearney et al. (2012), the addition of de-nitrification and burial terms (Fennel et al., 2009; Dunne et al., 2007), and the addition of sediment pools for PON and Opal. The sediment pools capture the detrital material that is not fully re-mineralized in the shallow water column of the eastern Bering Sea. The portion of material trapped in the sediment pools that is not buried (or de-nitrified) continues to re-

mineralize at the same rate as sinking particles in the water column.

The model domain extends from 20°N to 71°N and approximately 2250km offshore from the North American coast. The horizontal resolution is approximately 10km. There are 50 vertical levels with refinements at the surface and bottom layers. The bathymetry is generated by merging several bottom sounding data sets and mapping them on to 1–km wide grid cells (Danielson et al., 2011). In this paper we focus our analysis on model results at the mooring locations shown in Fig. 1.

The model was integrated from January 1987 to December 2007; 5-day averages of modeled fields were archived and used in our analyses. The physical initial and boundary conditions are derived from the Simple Ocean Data Assimilation (SODA) retrospective analysis (Carton and Giese, 2008). Nutrient initial and boundary conditions are derived from the World Ocean Atlas (WOA; Garcia et al., 2013). The surface forcing was derived from the Modern Era Retrospective Analysis for Research and Applications (MERRA) reanalysis (Rienecker et al., 2011). Three-hourly winds, air temperature, sea level pressure and specific humidity, daily short-wave and downwelling long-wave radiation fluxes and precipitation were used to compute air-sea heat and momentum fluxes using bulk formulae (Large and Yeager, 2009).

River discharge was implemented as a surface fresh water flux using the global river flow and continental discharges estimated by Dai and Trenberth (2002). Tidal forcing is implemented through the boundaries using the eight dominant diurnal and semi-diurnal components derived from the Oregon State Tidal Prediction Software (Egbert and Erofeeva, 2002).

2.3 Analysis Metrics

Ice retreat in the model simulation is defined as the last time before day 200 (July 17) that ice concentration on each grid cell falls below 15%. If ice in the model is not present at a mooring location during a year, ice retreat is defined as zero for that year. This will be compared with satellite data derived ice retreat presented in Sigler et al. (2014) where ice retreat is the last time before day 180 when ice concentration around each mooring is below 15%. We use day 200 in the model diagnosis to align with modeled spring bloom timing, but our results are not sensitive to this choice, as we shall see in the Results section.

To compare with the mooring chlorophyll-a observations, modeled total phytoplankton (summation of small and large phytoplankton, in units of mmol N/m^3) at 10-m depth is converted to units of mg Chl/m^3 using the canonical Redfield ratio (moles C:moles N=106:16) and a mean carbon to chlorophyll ratio of 20 (mg C:mg Chl=20). While the carbon to chlorophyll ratio in the Bering Sea is influenced by nutrient and light availability, size fraction, bloom status and other factors, and can vary by as much as factor of 3 (e.g., Lomas et al., 2012), a relatively low ratio (i.e., chlorophyll rich cells) is typical for the spring and fall bloom periods of primary interest in this study. It is also recognized that a number of marine biogeochemical processes can lead to deviations from the canonical Redfield ratio (e.g., Arrigo 2005). A variable Redfield ratio is not considered in our calculation, and can contribute to some discrepancies in the modeled versus observed chlorophyll-a concentration.

The modeled spring bloom magnitude of a year is represented by the maximum 5-day average of chlorophyll-a concentration at 10-m depth before day 200 (July 17) and

fall bloom magnitude is represented by the maximum 5-day average of 10-m chlorophyll-a after day 230 (August 16). Modeled spring bloom day is the time before day 200 when the 5-day average of chlorophyll-a achieves its maximum value. Day 200 and day 230 in the above calculations are 20 days later than the observational thresholds, but the 30-day interval between them is the same as in Sigler et al. (2014). Using the observational thresholds in these calculations (day 180 and day 210) does not change the results at M2 and M4 locations. It would misrepresent a few years at the M5 and M8 locations where maximum spring blooms happened after day 180, but would not change the overall conclusions of the study. In addition to chlorophyll-a concentration at one water depth, we also examined the timing and maxima of total depth integrated net primary production (in units of mg C/m^2/day) (NPP) simulated by the model. NPP is a more direct measurement of biological productivity of the water column, and it removes uncertainties associated with grazing and other factors such as variable C:Chl ratio.

To quantify water column stability, we calculated the potential energy (PE) index as a function of water depth at the mooring locations, thus, $PE(z) = \int_0^z (\rho(z) - \overline{\rho(z)}) gz dz$, where g is gravitational acceleration, ρ is density of the seawater, and the overbar represents vertical averaging. $PE(z)$ is computed using the 5-day averages of modeled temperature and salinity.

The strength of surface wind mixing was represented by cube of the wind speed. We also computed the time rate of change ($\frac{\partial N}{\partial t}$) and horizontal advection ($\vec{u} \cdot \nabla N$) of NO_3 using the 5-day averages of model fields, where t is time, $\vec{u}$ is the horizontal velocity vector, $\nabla = (\frac{\partial}{\partial x}, \frac{\partial}{\partial y})$, and N represents NO_3 concentration.

Cross-correlation coefficients were computed to establish empirical relationships between processes. Throughout this study, the correlation coefficients are tested using student-t distribution and their P values are reported.

3. Results

3.1 Model-observation comparisons

Figure 2 shows the monthly climatology of ice cover at the mooring locations from satellite observations and ROMS-NEMURO NEP simulations. As in satellite observations, maximum ice cover in the model generally occurs in March. However, modeled sea-ice melts slower than the satellite observations during April-June. As a result, the mooring locations are usually ice-free in the satellite observation for the June mean conditions but still up to 20% ice-covered in the model. July is usually ice-free in model simulations. It is not entirely clear why ice melts too slowly in the model. It could be due to deficiencies in the ocean model physics (shallower than observed surface mixed layer, for example) or missing impacts of ice algae on sea-ice (for example, presence of ice algae influences light absorption and energy balance in the ice) because ice algae are not modeled in the ROMS-NEMURO NEP. The slower than observed spring melting is also seen in global climate models with much coarser horizontal resolutions (Cheng et al., 2014).

Modeled ice cover at the mooring locations exhibits strong inter-annual variability (Fig. 3). In the north (M8 and M5), spring ice is always present and retreats relatively late (after April or May) (Fig. 3e). In the south (M2 and M4), the presence of ice is more variable from year-to-year, and the timing of spring ice retreat varies significantly (Fig.

3e). The majority of the ice retreat at these locations happens before day 180, therefore if we were to use day 180 as the cut-off date in the modeled ice-retreat calculation, our results would not change significantly. In the overlapping years between the model simulation and mooring observations (1995-2007), the modeled mean ice retreat days averaged over years when ice is present are 82, 113, 148, and 162, respectively, for mooring locations M2, M4, M5, and M8, compared to 77, 89, 126, and 136 correspondingly in the satellite data. Consistent with the monthly climatology time series (Fig. 2), on average, sea ice retreats later in the model than in satellite observations by 5 days, 24 days, 22 days, and 26 days for locations M2 to M8, respectively. The model simulation is similar to observations, however, in that the modeled ice retreats substantially earlier in the south than in the north. The multi-year mean northward delay in ice retreat from M4 to M5 is 35 days in the model, compared to a delay of 37 days in the satellite observations. Likewise, the delay of ice retreat from M5 to M8 is 14 days in the model, compared to 10 days in the satellite data. Hence, from M4 northward, the delays in the ice retreat timing from the south to the north are well captured by the model.

The simulated seasonal evolution of the 10-m chlorophyll-a concentrations are generally within the range of mooring observations, although the simulation did not capture the few instances of very high chlorophyll-a concentration observed at that depth (Fig. 4). This is not surprising given the patchiness in chlorophyll-a spatial distributions (Brown et al., 2011). Previous studies show a strong influence of ice retreat on the timing of spring bloom on the EBS shelf (e.g., Brown and Arrigo, 2013; Stabeno et al., 2012b; Sigler et al., 2014): if sea ice is present after mid-March, an ice-edge bloom occurs relatively early in the year and follows ice retreat from the south to the north between

early April and mid-June. Otherwise, if ice is not present or if it is present but retreats before mid-March, spring primary production bloom on the EBS shelf usually occurs in late May to early June, subsequent to thermal stratification. During the overlapping years between the model simulation and satellite observations (1995-2007), at M2 the ice-free years in the model are 2001, 2003 through 2005, whereas in satellite observations the ice-free years are 1996, 2001, 2003 through 2005. At M4, the ice-free years are identical between the model and satellite data (2001 and 2005).

The relationship between ice retreat and spring bloom day in the model simulation is shown in Fig. 5. Early ice retreats (before day 75, or March 15) only occurred at mooring locations M2 and M4 and, in a manner consistent with observations, were associated with blooms occurring long after the sea-ice retreats. Quantitatively, averaging over all years when ice retreats early and combining the data at the M2 and M4 locations, the spring bloom in the model occurred on day 157 (June 5) (SE=5.2, n=10), compared to day 148 (May 27) (SE=3.5, n=11) in the mooring observations. When all years and mooring locations for which ice retreats after day 75 are combined, the model results exhibit a significant linear relationship ($R=0.81$, $df=66$, $p<0.0001$) between day of ice retreat and day of spring bloom (Fig. 5b). The corresponding regression slope and y-intercept in the model are 0.39 and 117, respectively, compared to 0.66 and 53 in the mooring observations (Sigler et al., 2014). Therefore both the model simulation and observations show that for years with late ice retreat, the ice retreat and spring bloom dates are correlated.

Similar to the mooring observations, a secondary bloom occurs in fall in the model simulation (Fig. 6a). The spring and fall bloom magnitudes over the entire

modeling period are significantly correlated at the M8 (R=0.47, P=0.016) and M5 (R=0.41, P=0.032) locations (Fig. 6b). The correlation over the entire modeling period is not significant at the M2 and M4 locations (Fig. 6b), although there are shorter periods when the spring and fall blooms appear to co-vary (for example, during years 1991-2005 at the M2 location). The modeled NPP of the water column (units: mg C/m^2/day) at the mooring locations (Fig. 7) gives a qualitatively similar seasonal evolution of biological productivity on the EBS middle shelf as seen from the modeled chlorophyll-a concentration. The modeled spring and fall NPPs are well separated at the M2 and M4 locations, but the intervals between the two seasons are shorter at the M5 and M8 locations. This is mainly because the modeled spring NPP occurs progressively later at higher latitudes while the fall NPP timing is more consistent between the south and the north. Similar to the situations for chlorophyll-a concentration, the modeled spring versus fall NPP are significantly correlated at all mooring locations (Fig. 8).

Taken together, the above results suggest that the multi-year integration of the ROMS-NEMURO NEP captures two key links in the EBS ecosystem: 1) the relationship between ice retreat and spring bloom timing and 2) the co-variability between spring and fall productivities. In the following section (3.2 Mechanisms), we use the model simulation to explore mechanisms contributing to this seasonal co-variability. In these analyses, NPP will be used because it is a better measure of water column productivity than chlorophyll-a concentration.

3.2 Mechanisms

Because wind mixing is important for bringing lower water column nutrients to the surface euphotic zone, we first examined the amount of wind mixing during spring versus fall. This analysis suggests there is no significant correlation between the spring and fall surface wind mixing at these locations (Fig. 9). The EBS middle shelf is well mixed during winter and early spring (Coachman, 1986), and spring productivity often benefits from weakened winds from the stormy winter season to allow the establishment of stratification (Ladd and Stabeno, 2012). On inter-annual time scales, spring wind mixing is found positively correlated with spring net community production (Mordy et al., 2008; Eisner et al. 2015). The situation reverses in the fall, when increased wind mixing is required to break down the stratification established in summer in order to supply nutrients to start the fall primary production. The differing roles of seasonal surface wind variability on spring versus fall production and the weak correlation between the spring and fall winds suggest that surface wind could not be the bridge connecting spring and fall productivity on the EBS shelf.

Next, we examine the correlation between the modeled seasonal NPP and two key nutrient components NO_3 and NH_4 as a function of depth and time of year (Fig. 10). As expected, spring NPP is highly correlated with NO_3 throughout the water column at the beginning of the season (indicated by area "A" on Fig. 10a), and with NH_4 (area "B" on Fig. 10b) and NO_3 (area "C" on Fig. 10a) in the lower water column *following* the spring production. This result is consistent with *in situ* measurements (e.g., Whiteledge et al., 1986; Mordy et al., 2008) showing large quantities of NH_4 are produced in the bottom layer following the spring bloom on the EBS middle shelf. Simulated NPP averaged over the fall season is significantly correlated with NO_3 in the lower layers prior to the fall

production (area “D” on Fig. 10c), and with NH_4 concentration later in the year (area “E” on Fig. 10d). The large overlap of areas “B”, “C”, and “D” suggests an important role of local recycling/regeneration of nutrients from spring production promoting subsequent fall production, but it does not rule out the potential importance of horizontal advection in supplying nutrients to these locations in time and space.

To examine the relative importance of horizontal advection versus local recycling/regeneration, we compare the climatological (averaged over all modeled years) local rate of change of NO_3 concentration versus horizontal advection of NO_3 (Fig. 11). Across all stations, the local rate of change of NO_3 concentration (left panels on Fig. 11) indicates a strong spring drawdown (the large negative rates around day 150 in the surface layer) associated with spring production, as well as the subsurface drawdown corresponding to the fall production. The vertical dipoles of positive and negative rates around day 300 (Fig. 11, left panels) are consistent with vertical mixing bringing nutrients up the water column. Beneath the spring production and slightly delayed relative to upper layer NO_3 drawdown are positive rates of NO_3 change, which persist into the fall season (reaching day 300).

The late spring-to-fall increase in NO_3 concentration below the surface layer generally is not explained by contributions from horizontal advection (right panels on Fig. 11). The latter shows negative contributions over much of this time period, with the exception at the M4 location. The horizontal advection of NO_3 also exhibits a seasonal variation: it is strong from winter to early spring and tends to be positive and weak from late spring to early fall months. The mean horizontal advection of NO_3 is stronger at the northern stations (M5 and M8) than at stations further south. At M8 and M5 during the

winter months, horizontal advection decreases nutrient concentration in the upper layers but increases it in the bottom layers. The negative contribution by advection in the upper layer implies transport of low-nutrient water to the location. The observed ocean currents at these stations exhibit large temporal variability, and are primarily offshore during the winter months (Stabeno et al., this issue). The opposite signs of advection at the surface and bottom layers during winter months at M8 and M5 do not imply simultaneous flows in opposite directions.

Observed fall chlorophyll-a in the EBS is strongly influenced by water column stability (Eisner et al., 2014). Using the 5-day average model data, we computed the PE index (see Section 2.3) over the entire year and as a function of water depth, and examined the cross-correlation between the PE index and fall production. From M2, M4 and M5, the fall NPP is negatively correlated with fall stratification of the lower water column (Fig. 12c-h). The lack of negative correlation at M8 (Fig. 12a) is associated with the linear trends in both variables at this location (Fig. 12b); if these linear trends are removed, the cross-correlation between the variable is negative (not shown). Overall, the negative correlation between fall stratification of the lower water column and fall primary production is consistent with a decrease in stratification due to mixing providing an injection of nutrients from the bottom layers to the euphotic zone and an increase in production.

4. Discussion

Cross-season co-variability of chlorophyll-a on the EBS middle shelf is observed in mooring measurements and in numerical simulations of the ROMS-NEMURO NEP.

Co-variability is also apparent in the simulated NPP. While the correlation is modest and varies in time and space, it is important that we understand potential mechanisms underlying this co-variability. It is not obvious what processes may be responsible since nutrients in the upper water column tend to be depleted by the spring bloom in this relatively shallow shelf.

Our results, as well as those of previous studies (e.g., Deal et al., 2008), point to the importance of water column re-mineralization for sustained seasonal productivity on the EBS shelf. This is supported by the fact that ocean currents on the EBS middle shelf are weak during spring and summer (Stabeno et al., 2012a), leading to a limited role of transport in generating this seasonal co-variability. However, the complexity of EBS physical oceanography and ecosystem means that the controlling mechanisms can vary with time and location.

While a useful tool for exploring mechanisms, model simulations continue to have systematic biases. Spring ice melt in the ROMS-NEMURO NEP is too slow compared to observations; slower ice melting would favor late ice retreat and, consequently, early ice-edge associated blooms. Because of this early start of spring production, the simulation could overestimate the effects of local regeneration/nitrification.

Another limitation of the model is that it underestimates to some extent the large variation in observed bloom magnitude. As mentioned previously, this may in part reflect unresolved patchiness in chlorophyll-a distributions by the model, but other sources of variability not captured by the model could also play a role. Likely candidates in this regard include variation in basin-scale nutrient properties not reflected in the domain

boundary conditions, and variations in grazer populations linked to zooplankton life cycle dynamics that are not resolved by NEMURO. The analyses herein have demonstrated the ability of local re-mineralization dynamics to create seasonal co-variability on the EBS middle shelf, but we have not explained the total bloom magnitude variations. More work is needed to a) parse the unexplained variance into small-scale patchiness versus unexplained variability that the model can hope to capture with improved forcing and dynamics, and b) consider additional potential drivers of bloom magnitude and its variations.

Primary production on the EBS shelf has important implications for secondary production and higher trophic levels (Hunt et al., 2002, 2011; Coyle et al., 2011). Early spring blooms associated with late ice retreats could be beneficial to large crustacean zooplankton species (Sigler et al., 2014). Under climate projections on decadal to centennial time scales, sea ice retreat in the EBS becomes progressively earlier, although such a signal has not yet been observed (Brown and Arrigo, 2013). If local regeneration is an important process for fall blooms as suggested by this study, changes in the spring ice retreat and bloom dynamics can have effects later in the year. Changes in ocean environment due to climate forcing can influence seasonal nutrient recycling (nitrification and decomposition coefficients are typically temperature-dependent), contributing to the impacts of climate forcing on the marine ecosystem (Mueter et al., 2011). The net effect of climate change on the Bering Sea ecosystem remains an active research area (see http://www.nprb.org/bering-sea-project for summaries of recent developments), and surprises may await us because of the multitude of factors involved (Sigler et al., 2010).

5. Conclusions

Before using the ROMS-NEMURO NEP simulation as a diagnostic tool, we compared the model simulation with observations of seasonal ice cover, ice retreat day, and the relationship between ice retreat and spring bloom timing across the EBS middle shelf. Despite the slower than observed mean sea-ice melting rate in the spring, the modeled south-to-north progression of ice retreat is quantitatively similar to observations. As in the case for observations, the simulation also shows a linear relationship between ice retreat and spring bloom timing when ice is present after March 15 (i.e., during years of late ice retreat).

Consistent with observations, modeled primary production at the mooring locations exhibits distinct spring versus fall bloom seasons. The two bloom seasons are particularly separated at the lower latitudes (M2 and M4) where spring blooms occur early compared to higher latitudes (M5 and M8). Similar to observations, the modeled spring and fall blooms tend to co-vary on inter-annual scales – that is, a strong fall bloom tends to occur after a strong spring bloom. Since the model simulations captures these aspects of observed EBS ecosystem variability, we use the model output to examine whether wind mixing, local nutrient recycling/regeneration, horizontal advection of nutrients, and/or water column stability contribute to such seasonal co-variability of primary productivity on the EBS shelf. The major findings from this study are:

- There is no significant correlation between the spring and fall surface wind mixing magnitudes. In other words, while surface wind mixing is an important mechanism for bringing bottom layer nutrients to the upper water column, it is not the mechanism tying the two seasons' productivity together.

- Local regeneration/recycling of the nutrients fueling spring production is important for spring-to-fall nutrient accumulation in the bottom layers at the middle shelf.
- Horizontal advection does not appear to be the dominant factor for supplying nutrients to the middle shelf during the spring-to-fall period.
- Fall primary production in the model is strongly influenced by the lower water column stability/stratification.

While this paper rules out several possible drivers of seasonal co-variability and suggests a role for local re-mineralization, more work is needed to understand the full drivers of bloom magnitude variability on seasonal and interannual time scales on the EBS.

Acknowledgments

We thank three anonymous reviewers and Thomas Van Pelt for their careful reviews and constructive comments, which helped improve the manuscript greatly. We also thank Dr. Sigler for providing the daily mooring fluorescence chlorophyll-a data. Support from NPRB and NOAA's North Pacific Climate Regimes and Ecosystem Productivity (NPCREP) program is gratefully acknowledged. This publication is partially funded by the Joint Institute for the Study of the Atmosphere and Ocean (JISAO) under NOAA Cooperative Agreement NA10OAR4320148, Contribution No. 2266, and by NSF awards ARC-0732771, ARC-0732428, ARC-0957985, and ARC-1107250. This research is contribution Eco-FOCI-0844 to NOAA's Ecosystems & Fisheries Oceanography Coordinated Investigations, and contribution 4177 to NOAA/Pacific Marine

Environmental Laboratory. This is the BEST-BSIERP Bering Sea Project publication number 168, NPRB publication number 550.

Figure Captions

Figure 1. Study area. Filled hexagons mark the M2, M4, M5, and M8 mooring locations on the Eastern Bering Sea middle shelf. Gray (white) area is land (ocean) in the ROMS-NEMURO NEP model. Thin black lines denote the 50-m and 200-m ocean depth in the model.

Figure 2. Monthly climatology of ice cover at M2 through M8 locations in the ROMS-NEMURO NEP simulation (thin black) and in satellite observations (thick black). Vertical shading indicates the 95% confidence limit. Both the model and satellite results are computed over years 1987-2007.

Figure 3. 5-day averages of ice cover at the mooring locations (a-d) and ice retreat day (e, black circles) from ROMS-NEMURO NEP simulation. Red (green) crosses in (e) correspond to the mean (median) ice retreat in years 1987-2007. Vertical dashed lines mark day 200 (July 17), which separates the spring-summer ice-covered season from the fall-winter ice-covered season.

Figure 4. 5-day averages of chlorophyll-a at 10-m depth (units: mg Chl /m^3) in years 1987-2007 at the M2, M4, M5, and M8 locations from the ROMS-NEMURO NEP simulation (green lines) and 5-day averages of mooring chlorophyll-a data for years 1995-2011(red lines). Blue downward arrow (cross) symbols denote spring (fall) bloom amplitudes represented by the maximum 5-day averages before (after) day 200 (230) in the model.

Figure 5. Scatterplots of modeled ice retreat and spring bloom days at each mooring location (a) and combining all mooring results with late ice retreat (b). Years when ice is absent at a mooring location are ignored in (a). The vertical dashed lines in (a) mark day 75 (March 15) which is the threshold used for early ice retreat; the diagonal lines in (a) are the 1:1 ratio to compare ice retreat and spring bloom days. The straight line in (b) represents the linear fit between modeled ice retreat and spring bloom days and its functional form and correlation coefficient are marked on the panel.

Figure 6. Modeled 5-day averages of chlorophyll-a at 10-m depth (units: mg Chl/m^3) at the mooring locations as functions of days (0-365) and years (1987-2007) (left panels). Vertical lines denote day 200 (July 17) and day 230 (August 17), the season thresholds used in this study. Downward arrows indicate day 180 and day 210, the season thresholds used by Sigler et al. (2014). Modeled spring (black lines, left ordinate) and fall (red lines, right ordinate) bloom amplitudes at the mooring locations and their cross-correlations (right panels).

Figure 7. Modeled 5-day averages of total depth integrated primary production (units: mg C/m^2/day) at M8 through M2 locations as functions of days (0-365) and years (1987-2007). Vertical dashed lines mark the spring versus fall primary production seasons. Spring (fall) seasons are defined by finding a 75-day (65-day) period centered on the maximum multi-year mean primary production values before (after) day 230.

Figure 8. Modeled spring (dashed lines) and fall (solid lines) seasonal mean primary

productions (units: mg C/m^2/day) at the M2 through M8 locations. Seasonal mean is obtained by averaging over each spring and fall season denoted by the vertical dashed lines on Fig. 7. Cross-correlation coefficients and their P-values between the curves are shown on each panel.

Figure 9. Surface wind speed cubed at M2 through M8 locations. Solid (dash) lines correspond to fall (spring) seasonal averages. The cross-correlation coefficients between the two curves and their P values are shown on each panel.

Figure 10. Modeled cross-correlation patterns between the spring primary production and (a) NO_3 and (b) NH_4 concentration in the ROMS-NEMURO NEP simulation; between the fall primary production and (c) NO_3 and (d) NH_4 concentration. Letters "A" through "E" referred to features discussed in Section 3.2. Only values above the 95% confidence limit are shaded. These are results at the M2 location and results at other mooring locations are qualitatively similar. Vertical dashed lines mark the season boundaries as in Fig. 7.

Figure 11. Multi-year mean amplitudes of: time rate of changes of NO_3 (left panels) and horizontal advection of NO_3 (right panels) at M2 through M8 locations in the ROMS-NEMURO NEP simulation. Unit is mmol NO_3/m^3/day. These patterns are computed using 5-day averages of modeled fields. Vertical dashed lines mark the season boundaries as in Fig. 7.

Figure 12. Modeled cross-correlation patterns between fall primary production and ocean stratification of the entire year at M2 through M8 locations (a, c, e, g) and normalized fall primary production and fall stratification from surface to 40-meter depth (b, d, f, h). Only values above the 95% confidence limit are shown in a), c), e), g).

References

Arrigo, K.R., 2005. Marine microorganisms and global nutrient cycles, *Nature*, 437, 349–355.

Banas and co-authors, this issue. Past and future variability in spring plankton dynamics in the Eastern Bering Sea, 1971-2050.

Brown, Z.W., van Dijken, G.L., Arrigo, K.R., 2011. A reassessment of primary production and environmental change in the Bering Sea. *J. Geophys. Res. Oceans*, 116*,* C08014, http://dx.doi.org/10.1029/2010JC006766.

Brown, Z.W., Arrigo, K.R., 2013. Sea ice impacts on spring bloom dynamics and net primary production in the Eastern Bering Sea. *J. Geophys. Res. Oceans*, 118**,** 43–62.

Budgell, W., 2005. Numerical simulation of ice-ocean variability in the Barents Sea region: Towards dynamical downscaling, *Ocean Dynamics*, doi:10.1007/s10236-005-0008-3.

Carton, J.A., and B.S. Giese, 2008. A reanalysis of ocean climate using Simple Ocean Data Assimilation (SODA). *Mon. Wea. Rev.*, 136, 2999-3017.

Cheng, W., Curchitser, E., Ladd, C., Stabeno, P., Wang, M., 2014. Influences of sea ice on the Eastern Bering Sea: NCAR CESM simulations and comparison with observations. *Deep-Sea Res. II*, 109, 27-38.

Coachman, L.K., 1986. Circulation, water masses and fluxes on the southeastern Bering Sea shelf. *Cont. Shelf Res.* 5(1–2), 23–108.

Coachman, L. and V. Shigaev, 1992. Northern Bering-Chukchi Sea ecosystem: the physical basis. in Nagel, P. (ed.) *Results of the Third Joint US-USSR Bering and Chukchi Seas Expedition (BERPAC)*, *Summer 1988*. U.S. Fish and Wildlife Service,

Washington, D.C., pp. 17-27.

Comiso, J. C., 2000, updated 2014, Bootstrap Sea Ice Concentrations from Nimbus-7 SMMR and DMSP SSM/I-SSMIS. Version 2. Final-GSFC, northern hemisphere, Boulder, Colorado USA: NASA DAAC at the National Snow and Ice Data Center.

Coyle, K.O., Eisner, L.B., Mueter, F.J., Pinchuk, A.I., Janout, M.A., Cieciel, K.D., Farley, E.V., Andrews, A.G., 2011. Climate change in the southeastern Bering Sea: Impacts on pollock stocks and implications for the oscillating control hypothesis, *Fish. Oceanogr.* 20(2), 139–156.

Curchitser, E. N., D. B. Haidvogel, A. J. Hermann, E. L. Dobbins, T. M. Powell and A. Kaplan, 2005. Multi-scale modeling of the North Pacific Ocean: Assesment and analysis of simulated basin-scale variability (1996-2003), *J. Geophys. Res.,* 110, C11021, doi:101029/2005JC002902.

Curchitser, E.N, K. Hedstrom, S. Danielson and T. J. Weingartner, 2010. Modeling of Circulation in the North Aleutian Basin. Department of Interior, OCS Study BOEMRE 2010-028.

Dai, A., and K. E. Trenberth, 2002: Estimates of freshwater discharge from continents: Latitudinal and seasonal variations. *J. Hydrometeorol.*, 3, 660-687.

Dai, A., T. Qian, K. E. Trenberth and J. D. Milliman, 2009. Changes in continental fresh-water discharge from 1948–2004, *J. Climate*, 22, 2773–2791.

Danielson, S., E. Curchitser, K. Hedstrom, T. Weingartner, and P. Stabeno, 2011. On ocean and sea ice modes of variability in the Bering Sea, *J. Geophys. Res. Oceans,* 116(C12), doi:10.1029/2011JC007389.

Deal, C.J., Meibing, J., Jia, W., 2008. The significance of water column nitrification in

the southeastern Bering Sea. Chin. *J. Polar Science*, 19(2), 185–192.

Dunne, J. P., J. L. Sarmiento, and A. Gnanadesikan, 2007. A synthesis of global particle export from the surface ocean and cycling through the ocean interior and on the seafloor, *Global Biogeochem. Cycles,* 21, GB4006, doi:10.1029/2006GB002907.

Egbert, G. D. and S. Y. Erofeeva, 2002. Efficient Inverse Modeling of Barotropic Ocean Tides, *J. Atmos. Ocean. Tech.*, 19, 183–204.

Eisner, L.B., Napp, J.M., Mier, K.L., Pinchuk, A.I., Andrews III, A.G., 2014. Climate-mediated changes in zooplankton community structure for the eastern Bering Sea. *Deep-Sea Res. II*, 109, 157-171, http://dx.doi.org/10.1016/j.dsr2.2014.03.004.

Eisner, L.B., J.C. Cann, C. Ladd, K. Cieciel, and C. Mordy, 2015. Late summer/early fall phytoplankton biomass in the Eastern Bering Sea: Spatial and temporal variations and factors affecting chlorophyll-a concentrations. *Deep-Sea Res. II*, submitted.

Fennel, K., D. Brady, D. DiToro, R. Fulweiler, W. S. Gardner, A. Giblin, M.J. McCarthy, A. Rao, S. Seitzinger, M. Thouvenot-Korppoo, C. Tobias, 2009. Modelling denitrification in aquatic sediments. *Biogeochemistry*, 93:159-178 DOI 10.1007/s10533-008-9270-z .

Fiechter J., A.M. Moore, C.A. Edwards, K.W. Bruland, E. Di Lorenzo, C.V. Lewis, T.M Powell, E.N. Curchitser and K. Hedstrom, 2009. A simple approach to model iron limitation on pri- mary production in the coastal Gulf of Alaska. *Deep-Sea Res. II,* doi:10.1016/j.dsr2.2009.02.010.

Fiechter, J., E. N. Curchitser, C. A. Edwards, F. Chai, N. L. Goebel, and F. P. Chavez, 2014. Air- sea CO2 fluxes in the California Current: Impacts of model resolution and coastal topography. *Global Biogeochem. Cycles*, 28. doi:10.1002/2013GB004683.

Garcia, H. E., R. A. Locarnini, T. P. Boyer, J. I. Antonov, O.K. Baranova, M.M. Zweng, J.R. Reagan, D.R. Johnson, 2014. *World Ocean Atlas 2013, Volume 4: Dissolved Inorganic Nutrients (phosphate, nitrate, silicate)*. S. Levitus, Ed., A. Mishonov Technical Ed.; NOAA Atlas NESDIS 76, 25 pp.

Gibson, G.A. and Spitz, Y.H., 2011. Impacts of biological parameterisation, initial conditions, and environmental forcing on parameter sensitivity and uncertainty in a marine ecosystem model for the Bering Sea. *Journal of Marine Systems*. 88, pp. 214-231.

Gibson, G. A., Coyle, K.O., Hedstrom, K, Curchitser, E. N, 2013. A modeling study to explore on-shelf transport of oceanic zooplankton in the Eastern Bering Sea. *Journal of Marine Systems*. Volume 121, p. 47-64

Hermann, A. J., E. N. Curchitser, D. B. Haidvogel and E. L. Dobbins. 2009a. A comparison of remote versus local influence of El Nino on the coastal circulation of the Northeast Pacific. *Deep Sea Research II*, doi:10.1016/j.dsr2.2009.02.005.

Hermann, A.J., S. Hinckley, E. L. Dobbins, D. B. Haidvogel, N. A. Bond, C. Mordy, N. Kachel and P. J. Stabeno. 2009b. Quantifying cross-shelf and vertical nutrient flux in the Gulf of Alaska with a spatially nested, coupled biophysical model. *Deep Sea Research II*, doi:10.1016/j.dsr2.2009.02.008.

Hermann, A. J., Gibson, G. A., Bond, N. A., Curchitser, E. N., Hedstrom, K., Cheng, W., Wang, M., Stabeno, P. J., Eisner L., Janout, M. (in press). A multivariate analysis of observed and modeled biophysical variability on the Bering Sea shelf: multidecadal hindcasts (1969-2009) and forecasts (2010-2040). *Deep Sea Research II: Topical Studies in Oceanography*.

Hollowed, A.B., Barbeaux, S.J., Cokelet, E.D., Farley, E., Kotwicki, S., Ressler, P.H., Spital, C., Wilson, C.D., 2012. Effects of climate variations on pelagic ocean habitats and their role in structuring forage fish distributions in the Bering Sea. *Deep-Sea Res. II,* 65–70, 230–250.

Hunke, E. C., 2001. Viscous-plastic sea ice dynamics with the EVP model: linearization issues, *J. Comp. Phys.*, 170, 18–38.

Hunke, E. C. and J. K. Dukowicz, 1997. An elastic-viscous-plastic model for sea ice dynamics, *J. Phys. Oceanogr.*, 27, 1849–1868.

Hunt, G.L., Stabeno, P., Walters, G., Sinclair, E., Brodeur, R.D., Napp, J.M., Bond, N.A., 2002. Climate change and control of the southeastern Bering Sea pelagic ecosystem. *Deep-Sea Res. II,* 49(26), 5821–5853.

Hunt, G.L. Coyle, K.O., Eisner, L.B., Farley, E.V., Heintz, R.A., Mueter, F., Napp, J.M., Overland, J.E., Ressler, P.H., Salo, S., Stabeno, P.J., 2011. Climate impacts on eastern Bering Sea foodwebs: A synthesis of new data and an assessment of the Oscillating Control Hypothesis. *ICES J. Mar. Sci.,* 68(6), 1230–1243, http://dx.doi.org/10.1093/icesjms/fsr036.

Jin and co-authors, 2006. Controls of the landfast ice-ocean ecosystem offshore Barrow, Alaska. *Annals of Galciology*, 44, 63-72.

Jin, M., C. Deal, J. Wang, V. Alexander, R. Gradinger, S. Saitoh, T. Iida, Z. Wan, and P. Stabeno, 2007. Ice-associated phytoplankton blooms in the southeastern Bering Sea, *Geophys. Res. Lett.*, *34*(6), L06612, doi:10.1029/2006GL028849.

Jin, M., C. Deal, J. Wang, and C. P. McRoy, 2009. Response of lower trophic level production to long-term climate change in the southeastern Bering Sea, *J. Geophys. Res. Oceans*, *114*(C4), C04010, doi:10.1029/2008JC005105.

Kearney, K., C. A. Stock, K Aydin, and J. L. Sarmiento, 2012. Coupling planktonic ecosystem and fisheries food web models for a pelagic ecosystem: Description and validation for the subarctic Pacific. *Ecological Modelling*, 237-238, DOI:10.1016/j.ecolmodel.2012.04.006.

Kishi and co-authors, 2007. NEMURO—a lower trophic level model for the North Pacific marine ecosystem. *Ecological Modeling*, 202, 12–25.

Ladd, C., Stabeno, P.J., 2012. Stratification on the Eastern Bering Sea shelf revisited. *Deep-Sea Res. II*, 65–70, 72–83.

Large, W. G. and S. G. Yeager, 2009. The global climatology of an interannually varying air-sea flux data set, *Clim. Dyn.*, 33, 341–364.

Lomas, M.W., Moran, S.B., Casey, J.R., Bell, D.W., Tiahlo, M., Whitefield, J., Kelly, R.P., Mathis, J.T., Cokelet, E.D., 2012. Spatial and seasonal variability of primary production on the Eastern Bering Sea shelf. *Deep-Sea Res. II*, 65–70, 126–140.

Mathis, J. T., J. N. Cross, N. R. Bates, S. Bradley Moran, M. W. Lomas, C. W. Mordy, and P. J. Stabeno, 2010. Seasonal distribution of dissolved inorganic carbon and net community production on the Bering Sea shelf, *Biogeosciences*, *7*(5), 1769–1787, doi:10.5194/bg-7-1769-2010.

Mellor, G. L. and L. Kantha, 1989. An ice-ocean coupled model, *J. Geophys. Res*., 94, 10, 937–10,954.

Mordy, C.W., P.J. Stabeno, D. Righi, and F.A. Menzia, 2008. Origins of the subsurface ammonium maximum in the southeast Bering Sea, *Deep-Sea Res. II*, 55, 1738-1744.

Mueter, F.J., Bond, N.A., Ianelli, J.N., Hollowed, A.B., 2011. Expected declines in recruitment of walleye pollock (*Theragra chalcogramma*) in the eastern Bering Sea under future climate change. *ICES J. Mar. Sci.*, 68(6), 1284–1296, http://dx.doi.org/10.1093/icesjms/fsr022.

Pease, C. H., 1980. Eastern Bering Sea Ice Processes, *Mon. Weather Rev.*, *108*(12), 2015–2023.

Rienecker, Michele M., and Coauthors, 2011: MERRA: NASA's Modern-Era Retrospective Analysis for Research and Applications. *J. Climate*, **24**, 3624–3648.

Shchepetkin, A. F. and J. C. McWilliams, 2005. The Regional Ocean Modeling System (ROMS): A split-explicit, free-surface, topography-following coordinates oceanic model, *Ocean Modelling*, 9, 347–404.

Sigler, M.F., Harvey, H.R., Ashjian, J., Lomas, M.W., Napp, J.M., Stabeno, P.J., Van Pelt, T.I., 2010. How does climate change affect the Bering Sea ecosystem? *Eos Trans. AGU*, 91(48), 457–458.

Sigler, M.F., Stabeno, P.J., Eisner, L.B., Napp, J.M., Mueter, F.J., 2014. Spring and fall phytoplankton blooms in a productive subarctic ecosystem, the eastern Bering Sea, during 1995–2011. *Deep-Sea Res. II,* 109, 71-83, doi:10.1016/j.dsr2.2013.12.007.

Springer, A. M., C. P. McRoy, and M. V. Flint, 1996. The Bering Sea Green Belt: shelf-edge processes and ecosystem production, *Fish. Oceanogr.*, *5*(3-4), 205–223.

Stabeno, P.J., Napp, J., Mordy, C., Whitledge, T., 2010. Factors influencing physical structure and lower trophic levels of the eastern Bering Sea shelf in 2005: Sea ice, tides and winds. *Prog. Oceanogr.*, 85(3–4), 180–196.

Stabeno, P.J., Farley Jr., E.V., Kachel, N.B., Moore, S., Mordy, C.W., Napp, J.M., Overland, J.E., Pinchuk, A.I., Sigler, M.F., 2012a. A comparison of the physics of the northern and southern shelves of the eastern Bering Sea and some implications for the ecosystem. *Deep-Sea Res. II,* 65–70, 14–30.

Stabeno, P.J., Kachel, N.B., Moore, S.E., Napp, J.M., Sigler, M., Yamaguchi, A., Zerbini, A.N., 2012b. Comparison of warm and cold years on the southeastern Bering Sea shelf and some implications for the ecosystem. *Deep-Sea Res. II,* 65–70, 31–45.

Stabeno, P.J., S. Danielson, D. Kachel, N. B. Kachel, C. Mordy, this issue. Currents and transports on the Eastern Bering Sea shelf.

Steele, M., G. L. Mellor and M. G. McPhee, 1989. Role of the molecular sublayer in the melting or freezing of sea ice, *J. Phys. Oceanogr.,* 19, 139–147.

Sullivan, M. E., N. B. Kachel, C. W. Mordy, S. A. Salo, and P. J. Stabeno, 2014. Sea ice and water column structure on the eastern Bering Sea shelf, *Deep Sea Res. II, 109*, 39–56, doi:10.1016/j.dsr2.2014.05.009.

Whitledge, T.E., Reeburgh, W.S., Walsh, J.J., 1986. Seasonal inorganic nitrogen distributions and dynamics in the southeastern Bering Sea. *Cont. Shelf Res.*, 5(1–2), 109–132.

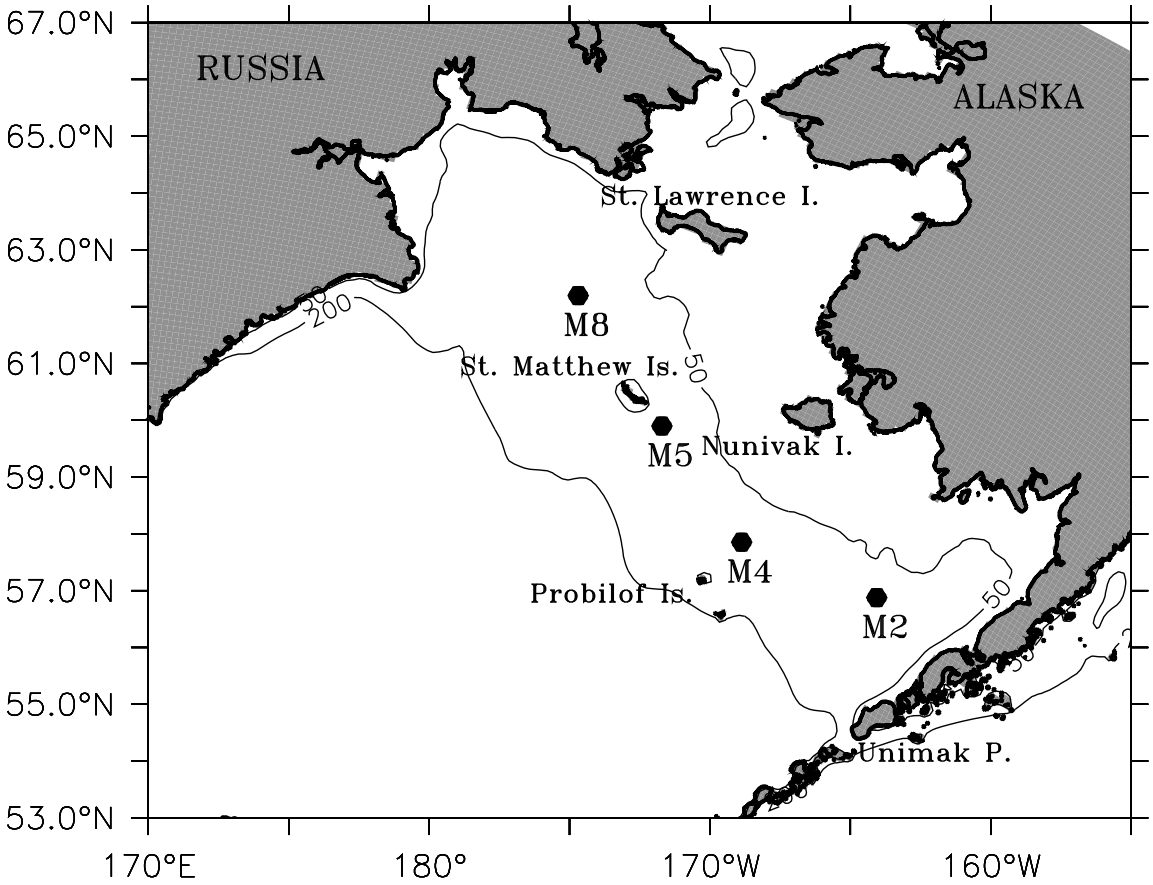

Fig. 1. Study area. Filled hexagons mark the M2, M4, M5, and M8 mooring locations on the Eastern Bering Sea middle shelf. Gray (white) area is land (ocean) in the ROMS-NEMURO NEP model. Thin black lines denote the 50-m and 200-m ocean depth in the model.

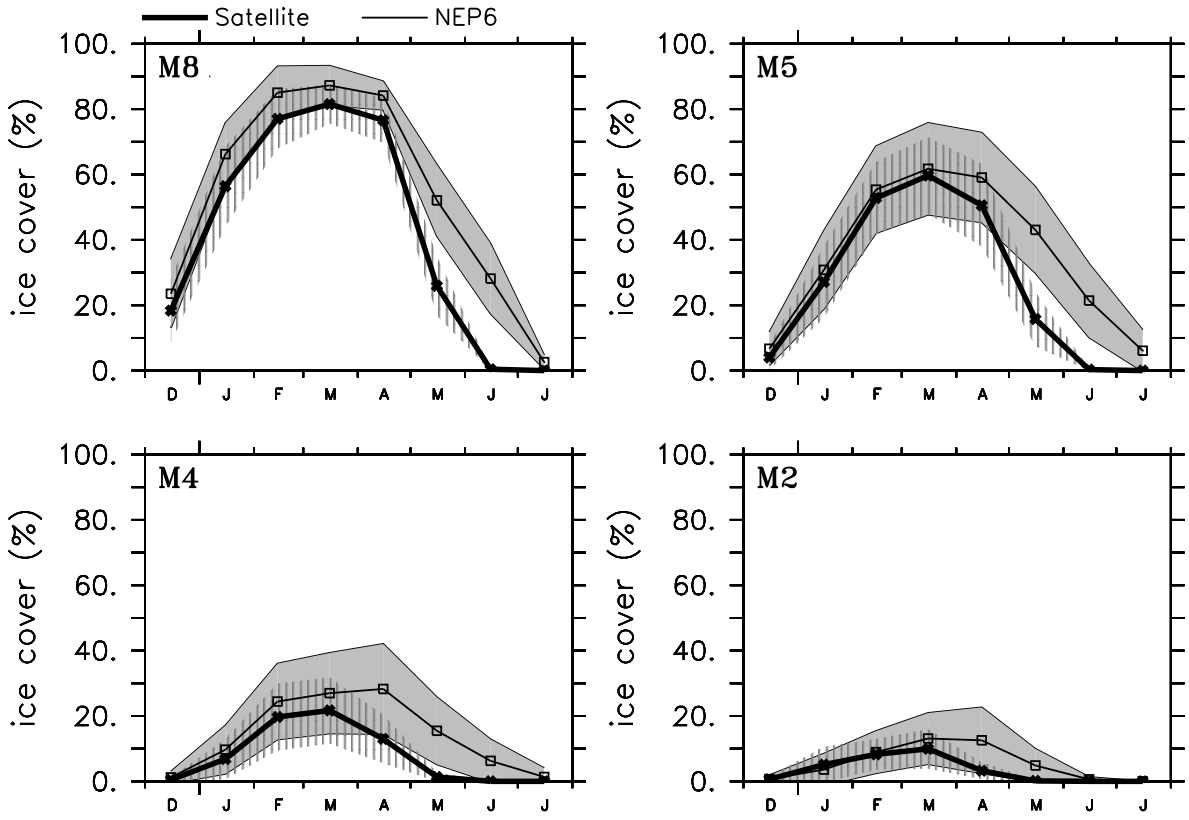

Fig. 2. Monthly climatology of ice cover at M2 through M8 locations in the ROMS-NEMURO NEP simulation (thin black) and in satellite observations (thick black). Vertical shading indicates the 95% confidence limit. Both the model and satellite results are computed over years 1987-2007.

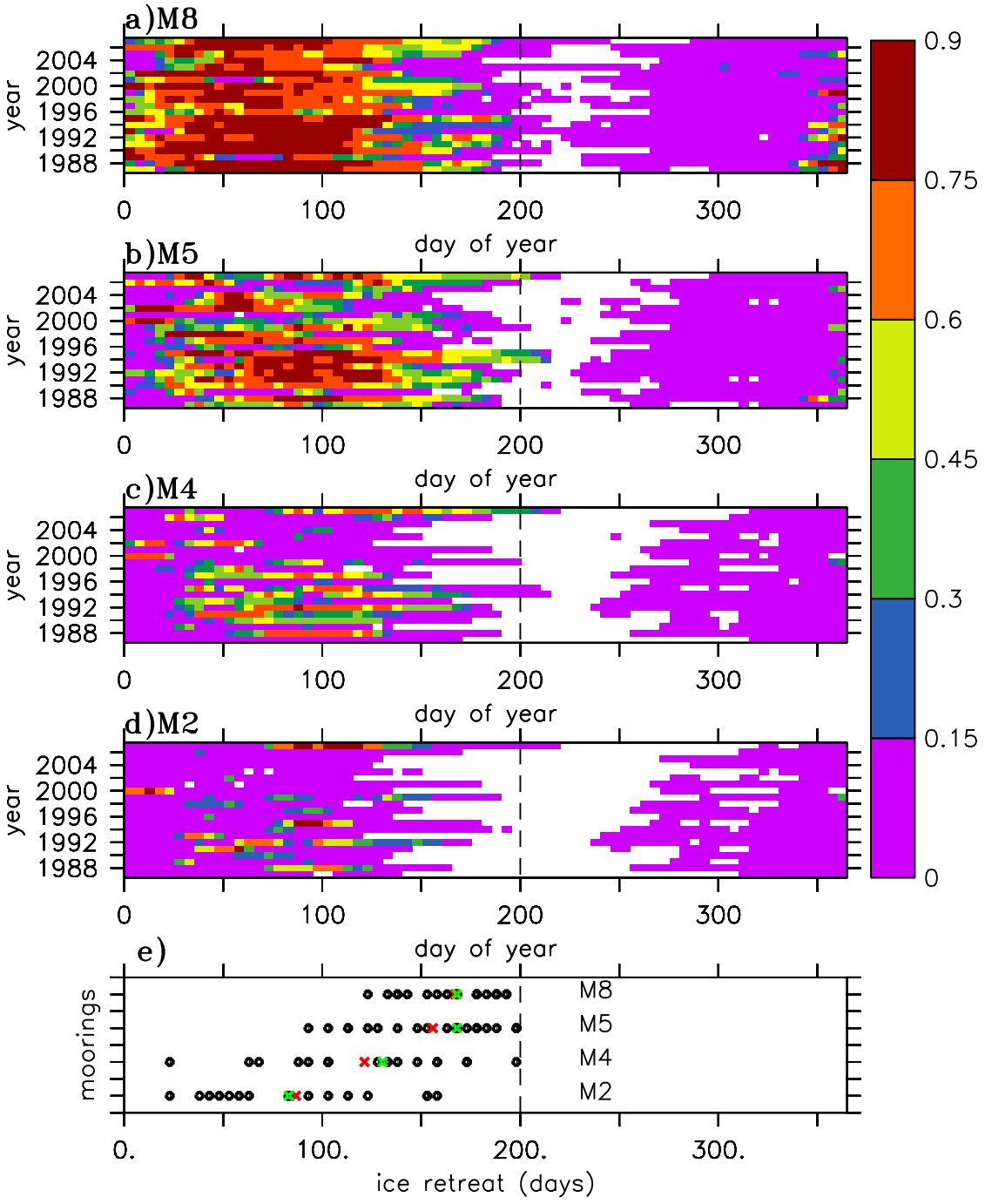

Fig. 3. 5-day averages of ice cover at the mooring locations (a-d) and ice retreat day (e, black circles) from ROMS-NEMURO NEP simulation. Red (green) crosses in (e) correspond to the mean (median) ice retreat in years 1987-2007. Vertical dashed lines mark day 200 (July 17), which separates the spring-summer ice-covered season from the fall-winter ice-covered season.

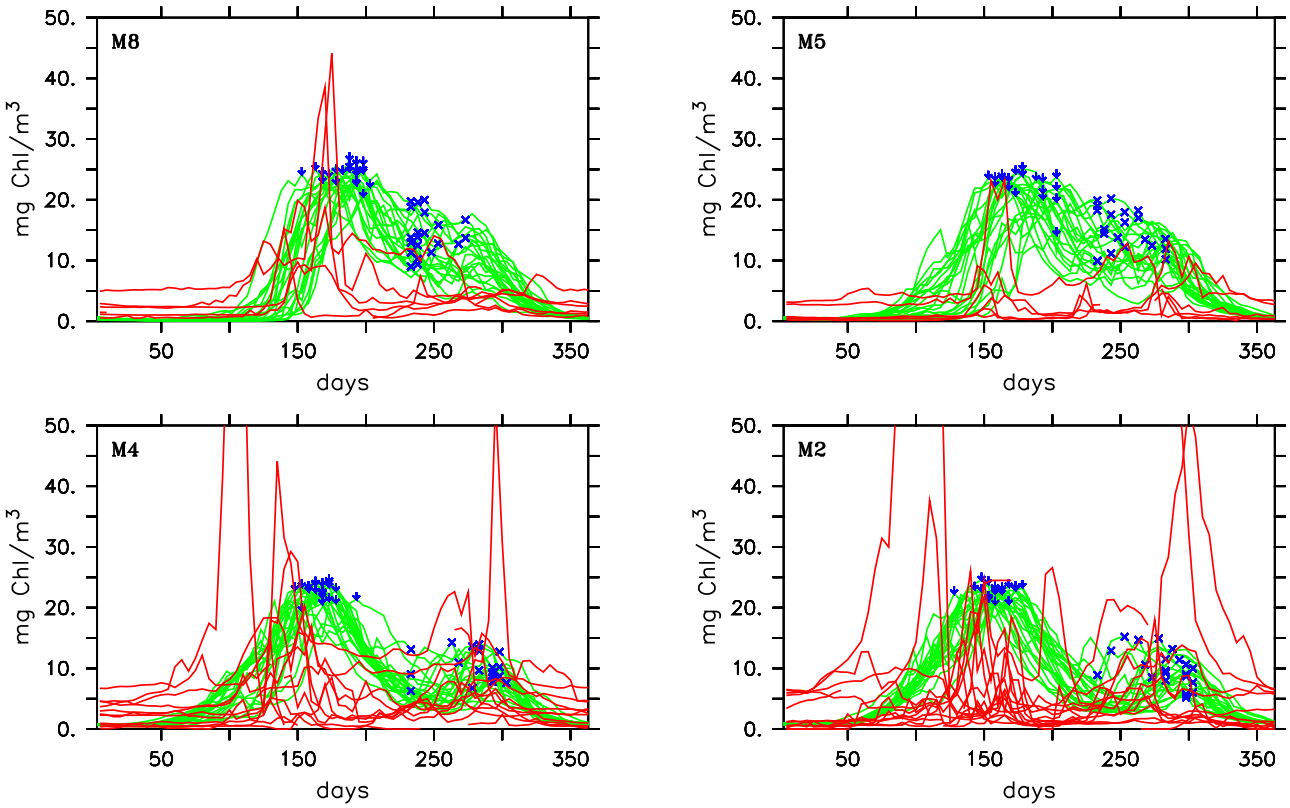

Fig. 4. 5-day averages of chlorophyll-a at 10-m depth (units: mg Chl /m^3) in years 1987-2007 at the M2, M4, M5, and M8 locations from the ROMS-NEMURO NEP simulation (green lines) and 5-day averages of mooring chlorophyll-a data for years 1995-2011(red lines). Blue downward arrow (cross) symbols denote spring (fall) bloom amplitudes represented by the maximum 5-day averages before (after) day 200 (230) in the model.

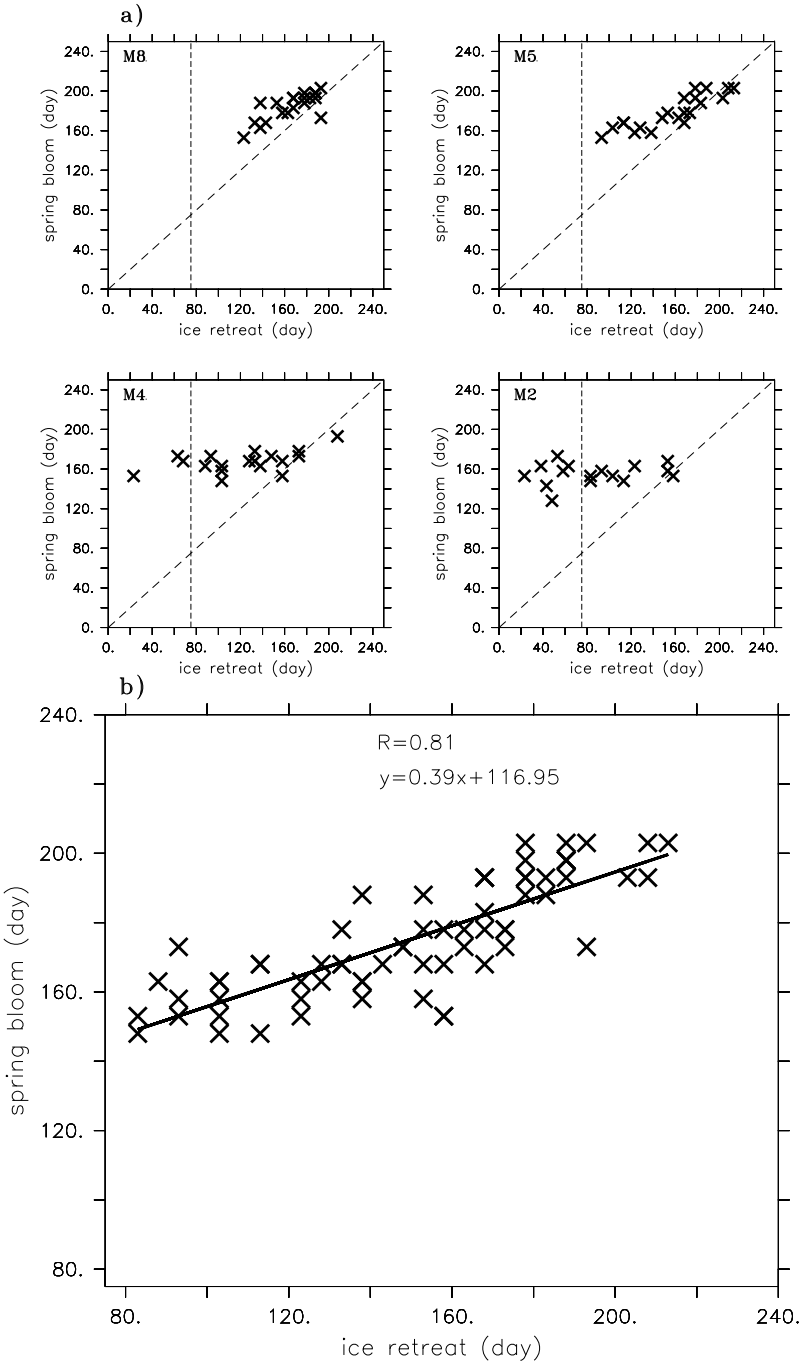

Fig. 5. Scatterplots of modeled ice retreat and spring bloom days at each mooring location (a) and combining all mooring results with late ice retreat (b). Years when ice is absent at a mooring location are ignored in (a). The vertical dashed lines in (a) mark day 75 (March 15) which is the threshold used for early ice retreat; the diagonal lines in (a) are the 1:1 ratio to compare ice retreat and spring bloom days. The straight line in (b) represents the linear fit between modeled ice retreat and spring bloom days and its functional form and correlation coefficient are marked on the panel.

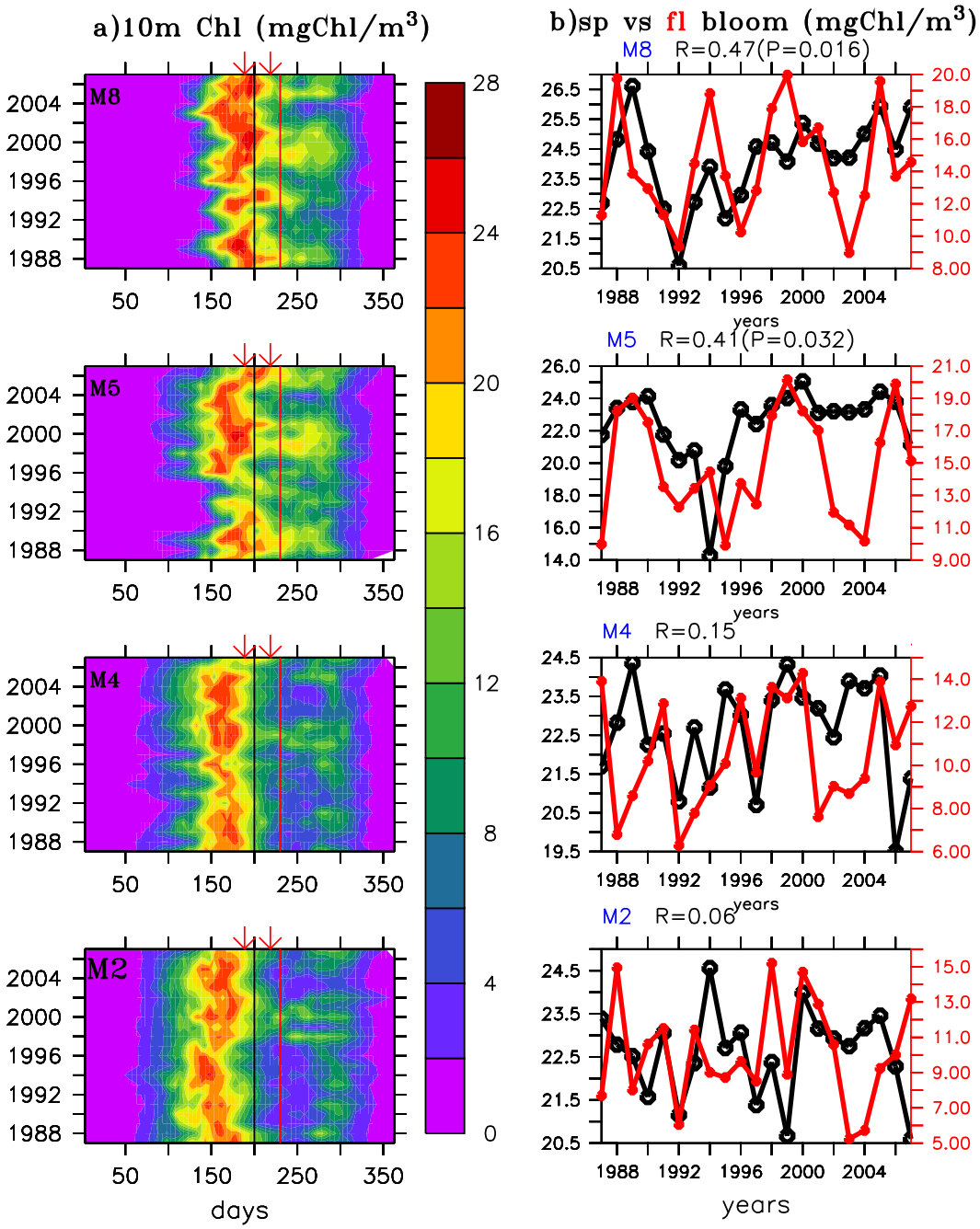

Fig. 6. Modeled 5-day averages of chlorophyll-a at 10-m depth (units: mg Chl/m^3) at the mooring locations as functions of days (0-365) and years (1987-2007) (left panels). Vertical lines denote day 200 (July 17) and day 230 (August 17), the season thresholds used in this study.Downward arrows indicate day 180 and day 210, the season thresholds used by Sigler et al. (2014). Modeled spring (black lines, left ordinate) and fall (red lines, right ordinate) bloom amplitudes at the mooring locations and their cross-correlations (right panels).

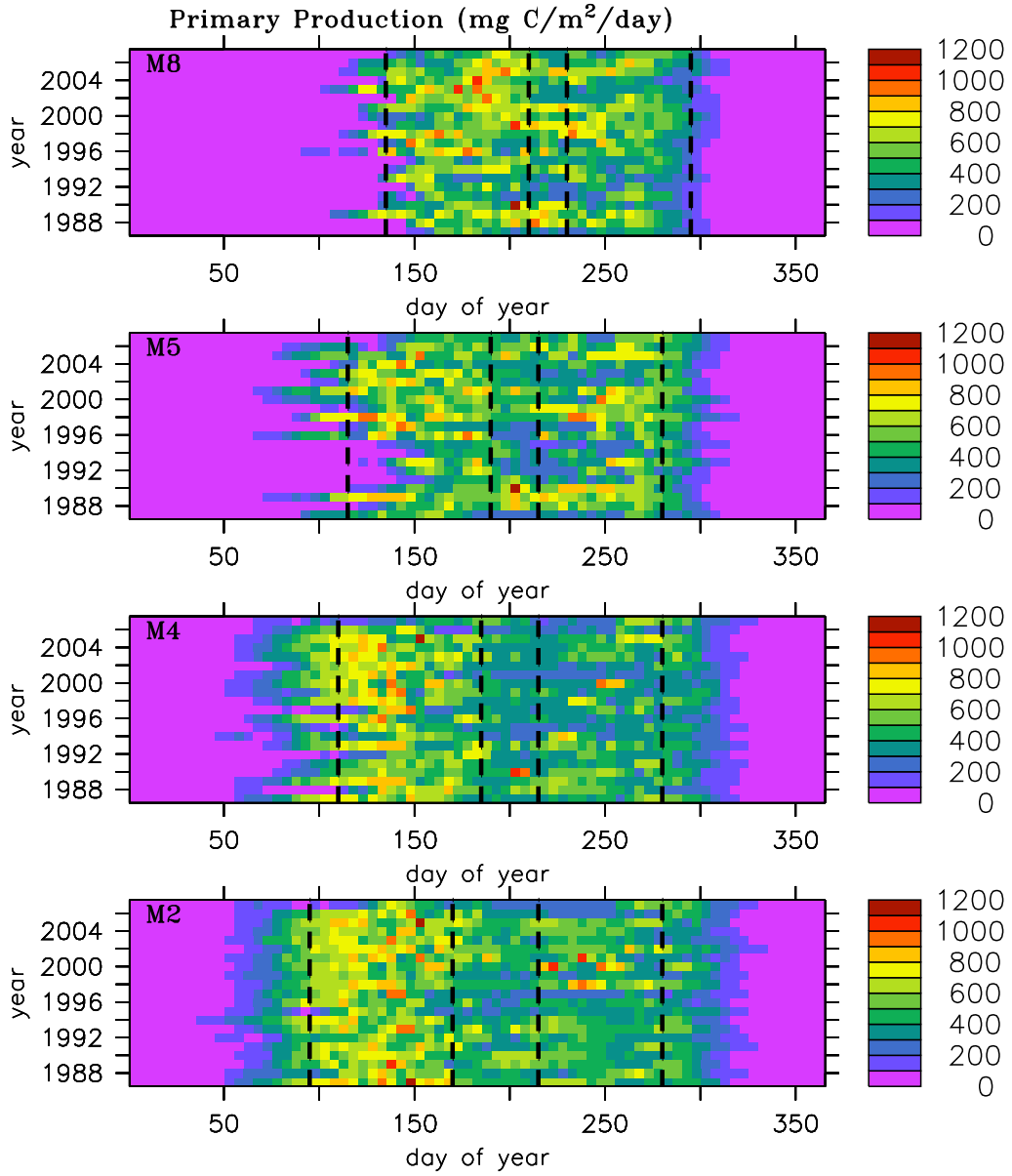

Fig. 7. Modeled 5-day averages of total depth integrated primary production (units: mg C/m^2/day) at M8 through M2 locations as functions of days (0-365) and years (1987-2007). Vertical dashed lines mark the spring versus fall primary production seasons. Spring (fall) seasons are defined by finding a 75-day (65-day) period centered on the maximum multi-year mean primary production values before (after) day 230.

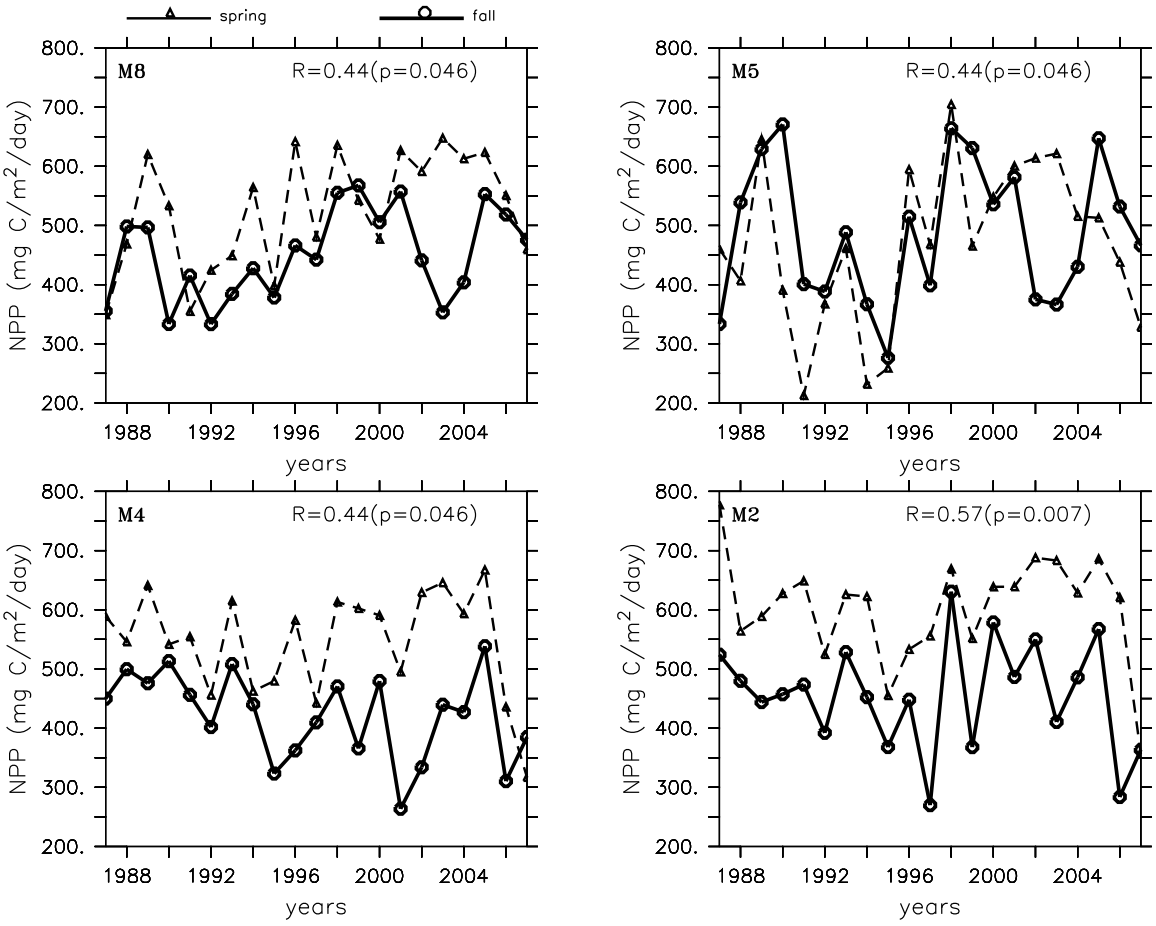

Fig. 8. Modeled spring (dashed lines) and fall (solid lines) seasonal mean primary productions (units: mg C/m^2/day) at the M2 through M8 locations. Seasonal mean is obtained by averaging over each spring and fall season denoted by the vertical dashed lines on Fig. 7. Cross-correlation coefficients and their P-values between the curves are shown on each panel.

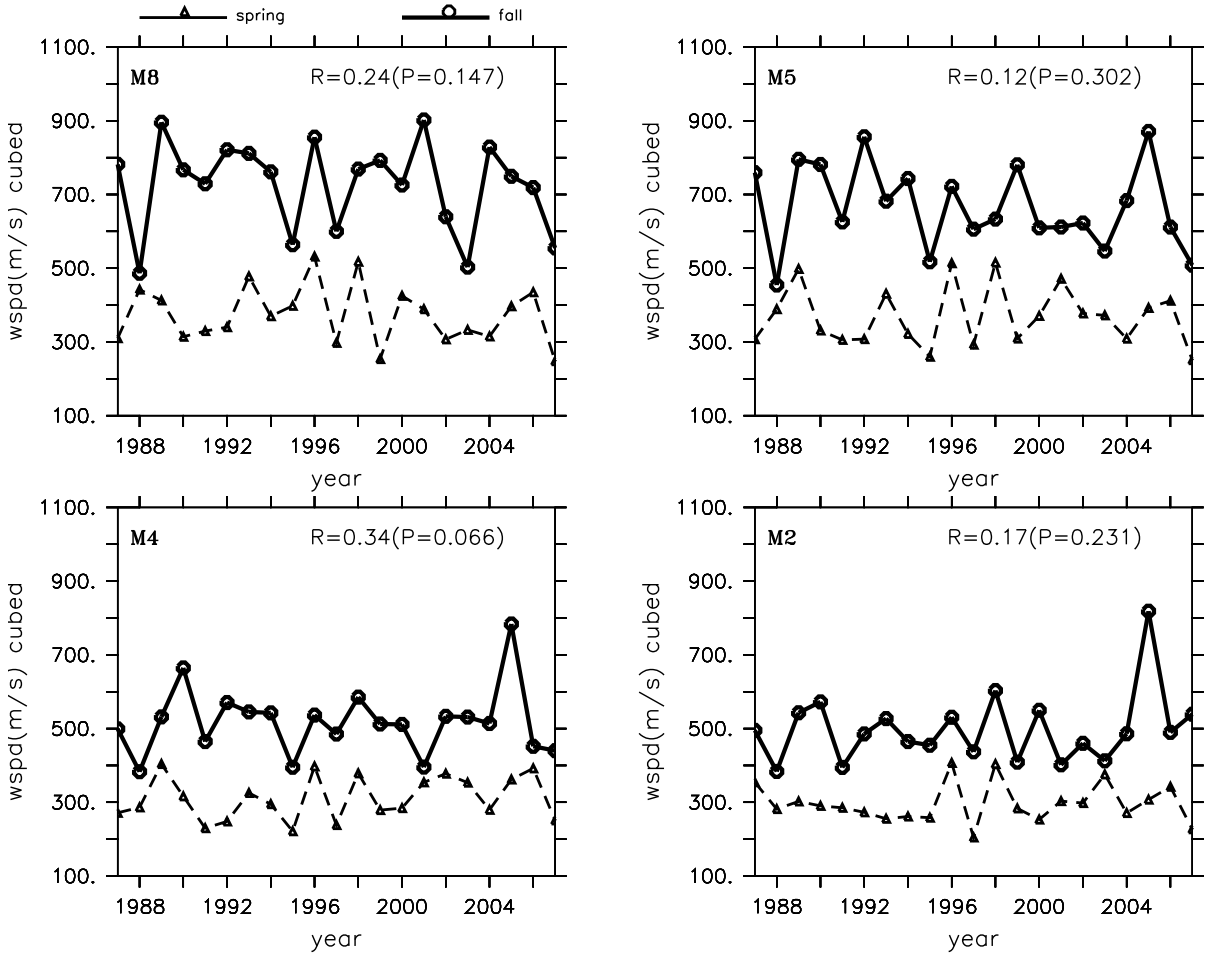

Fig. 9. Surface wind speed cubed at M2 through M8 locations. Solid (dash) lines correspond to fall (spring) seasonal averages. The cross-correlation coefficients between the two curves and their P values are shown on each panel.

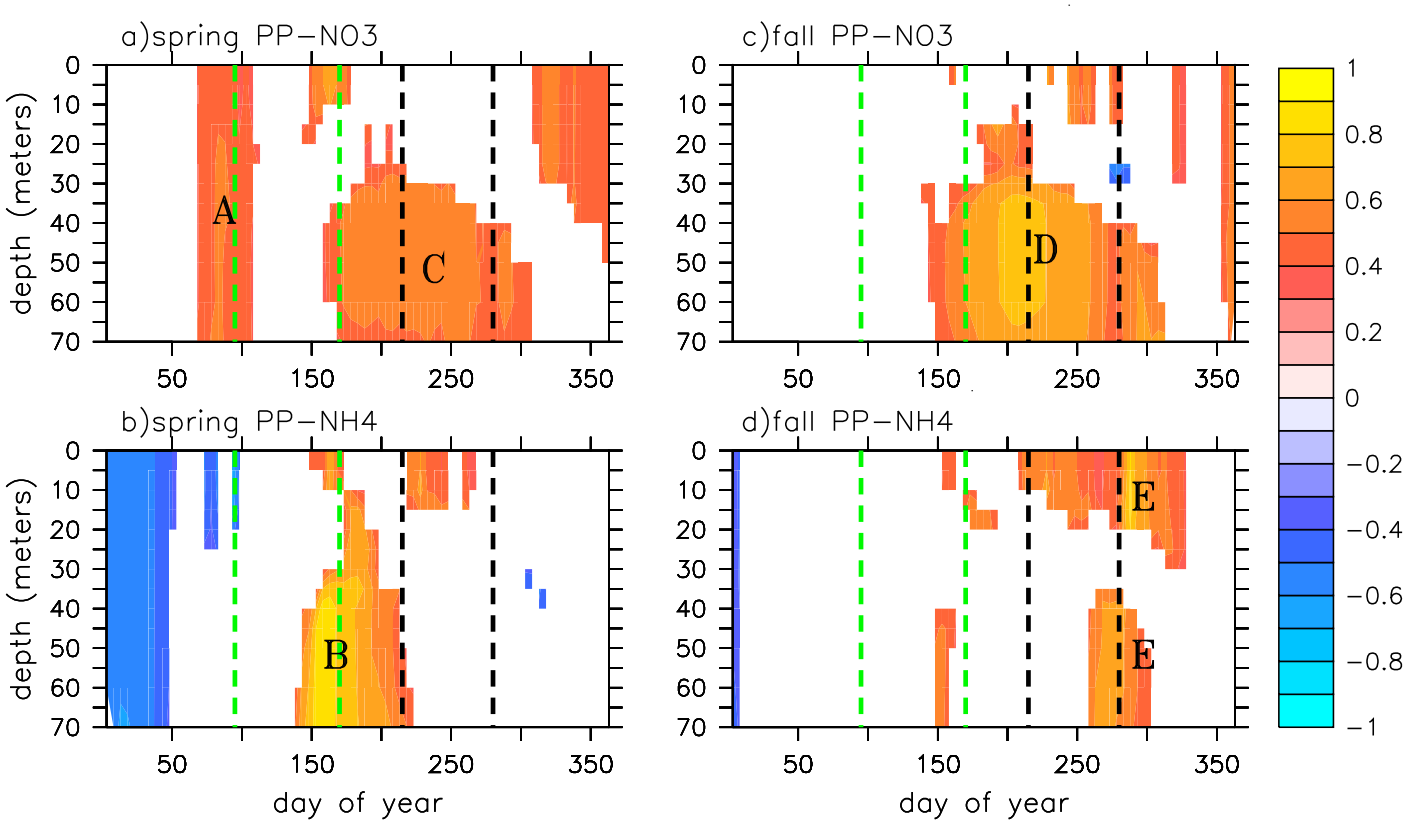

Fig. 10. Modeled cross-correlation patterns between the spring primary production and (a) NO_3 and (b) NH_4 concentration in the ROMS-NEMURO NEP simulation; between the fall primary production and (c) NO_3 and (d) NH_4 concentration. Letters "A" through "E" referred to features discussed in Section 3.2. Only values above the 95% confidence limit are shaded. These are results at the M2 location and results at other mooring locations are qualitatively similar. Vertical dashed lines mark the season boundaries as in Fig. 7.

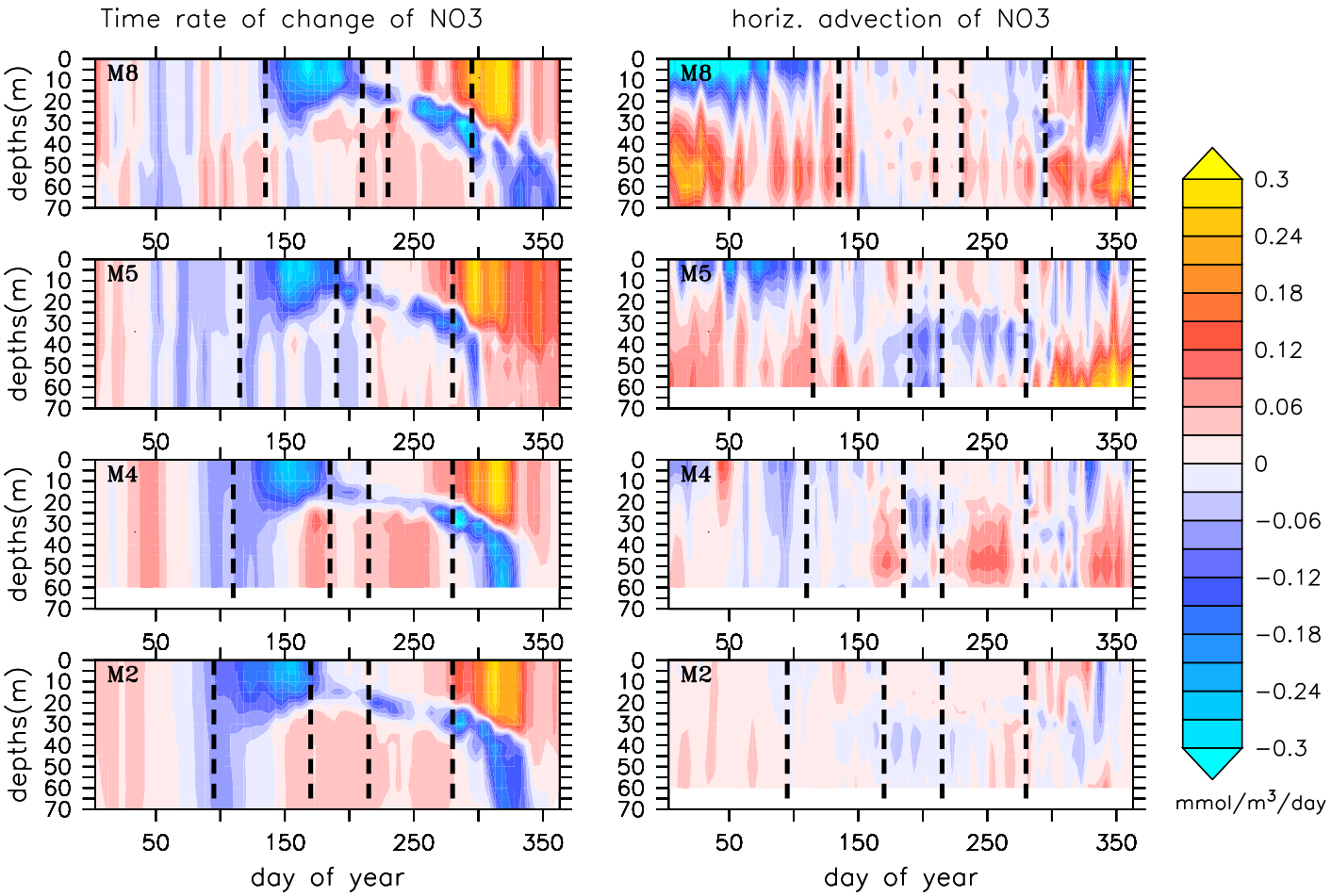

Fig. 11. Multi-year mean amplitudes of: time rate of changes of NO_3 (left panels) and horizontal advection of NO_3 (right panels) at M2 through M8 locations in the ROMS-NEMURO NEP simulation. Unit is mmol NO_3/m^3/day. These patterns are computed using 5-day averages of modeled fields. Vertical dashed lines mark the season boundaries as in Fig. 7.

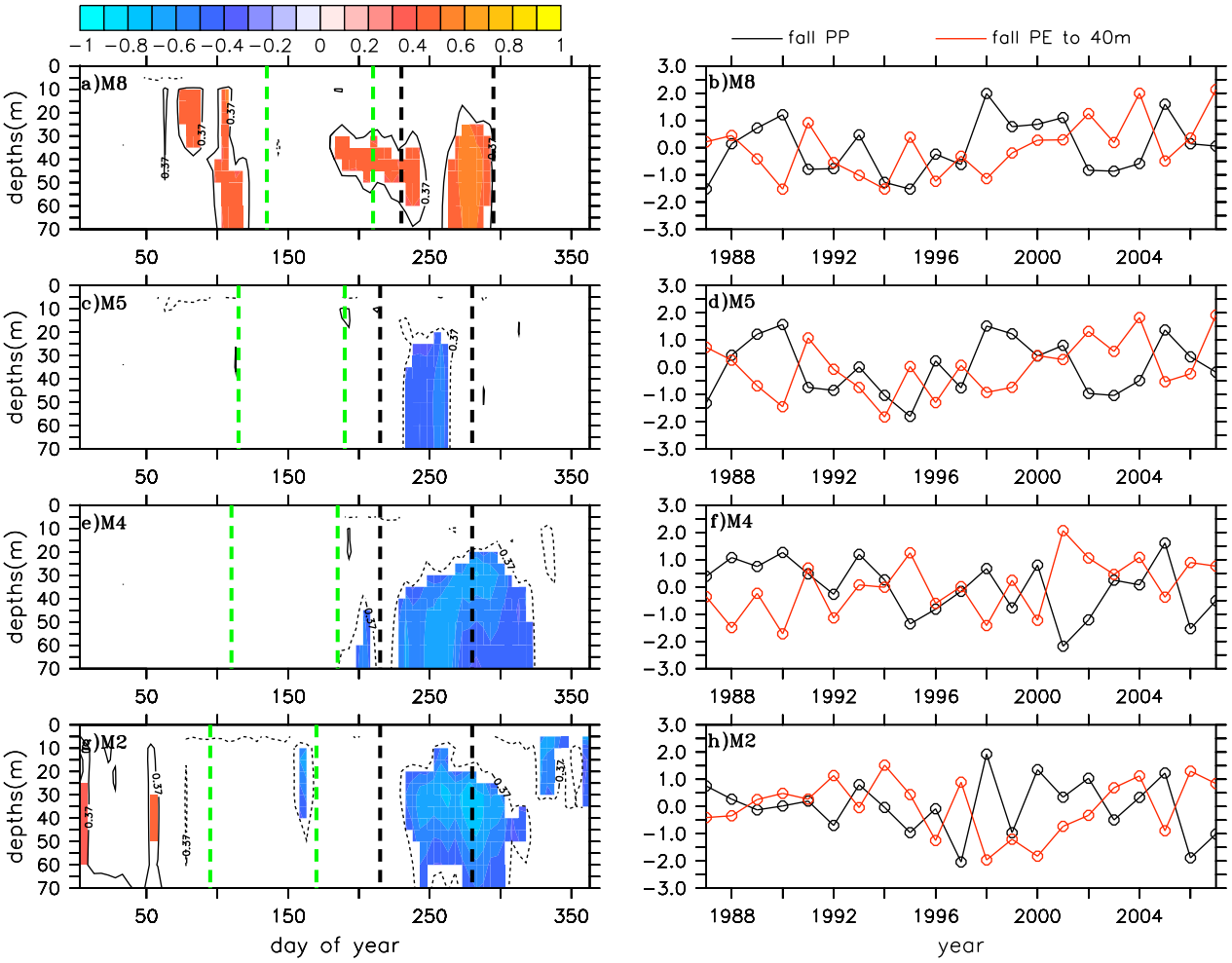

Fig. 12. Modeled cross-correlation patterns between fall primary production and ocean stratification of the entire year at M2 through M8 locations (a, c, e, g) and normalized fall primary production and fall stratification from surface to 40-meter depth (b, d, f, h). Only values above the 95% confidence limit are shown in a), c), e), g).